

# Supplementary Information

**“Moraine crest or slope: an analysis of the effects of boulder position on cosmogenic exposure age”**

Tomkins *et al.* (2020)

*link to doi here*

## 1 | Description

This supplementary file describes the contents of the following data tables:

1. “**Supplementary\_Table\_1\_10Be.csv**”. This file includes  $^{10}\text{Be}$  sample information used for TCN exposure age calculation. The data are listed in the format required for the CRONUS Earth Web Calculator (Version 2.0; Marrero et al. (2016), available at: <http://cronus.cosmogenicnuclides.rocks/2.0/>). Required variables and their descriptions are available here: <http://cronus.cosmogenicnuclides.rocks/2.0/html/al-be/CRONUScalc26Al10BeTemplate.xlsx>, with additional information in Section 2.1.
2. “**Supplementary\_Table\_2\_36Cl.csv**”. This file includes  $^{36}\text{Cl}$  sample information used for TCN exposure age calculation, in the format described above. Required variables and their descriptions are available here: <http://cronus.cosmogenicnuclides.rocks/2.0/html/cl/CRONUScalc36ClTemplate.xlsx>, with additional information in Section 2.1.
3. “**Supplementary\_Table\_3\_SH.csv**”. This file includes sample information for all boulders sampled using the Schmidt hammer ( $n = 645$ ). Variable names and calculation steps are described in Section 2.2.

**Section 3** comprises a pseudo code description of the Monte Carlo simulated Orthogonal Distance Regression. The full Python implementation is available on GitHub: [https://github.com/matt-tomkins/moraine\\_paper\\_2020](https://github.com/matt-tomkins/moraine_paper_2020).

**Section 4** describes the sampling approach on the Arànsa right moraine and laboratory procedures for  $^{10}\text{Be}$  sample preparation and measurement.

# 2 | Variable names

## 2.1 Supplementary Tables 1-2

Columns [6:36] $(^{10}\text{Be})$  and [6:84] $(^{36}\text{Cl})$  are in the format required by the CRONUS Earth Web Calculator (Marrero et al., 2016). The remaining variables are described below:

### Group

Identifier to distinguish different exposure age groups, as described below:

- “Calibration **dataset**” = The 52  $^{10}\text{Be}$  dated surfaces used in Tomkins et al. (2018a).
- “Calibration **outlier**” = Outliers ( $n = 2$ ; see Fig. 2.1A-B), excluded by Tomkins et al. (2018a). These samples are likely compromised by prior exposure (inheritance). These include sample CAC28 from the Cometa d’Espagne cirque (Crest et al., 2017), which is proximal (~2 m) to three tightly clustered bedrock ages (c. 11 - 12 ka; mean squared weighted deviation [MSWD] = 0.094). Similarly, sample ICM04 from the Malniu catchment (Pallàs et al., 2010) is proximal (~10m) to three dated moraine boulders (c. 40 - 50 ka; MSWD = 0.945). When these outliers are removed, both of these data sets are internally consistent (MSWD < 1).
- “Calibration **new**” = This includes two additional  $^{10}\text{Be}$  ages from the Noguera Ribagorçana (MUL01 and MUL03; Pallàs et al., 2006) which were sampled with the Schmidt hammer during recent fieldwork (see Fig. 2.1C-D).
- “New moraine samples” = This includes all  $^{10}\text{Be}$  and  $^{36}\text{Cl}$  samples from the studied moraines ( $n = 19$ ; Pallàs et al., 2006; Rodés, 2008; Palacios et al., 2015), of which 15 were sampled with the Schmidt hammer.

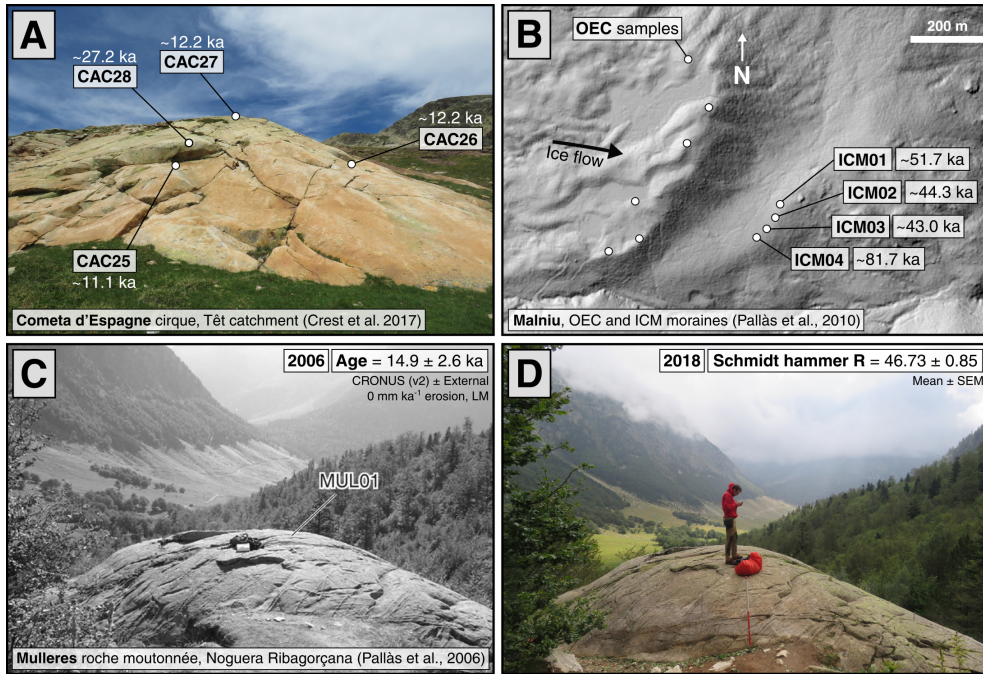


Figure 2.1: Outliers (A-B) and new calibration data (C-D) for the Pyrenean TCN-SH calibration curve (Tomkins et al., 2018a). (A) Outlier sample CAC28 from the Cometa d'Espagne cirque (Crest et al., 2017). (B) Outlier sample ICM04 from Malniu (Pallàs et al., 2010). (C) Sample photograph (2006) for new calibration sample MUL01 from the Noguera Ribagorçana (Pallàs et al., 2006) and its calculated surface exposure age ( $\pm$  external age uncertainty; CRONUS Earth Web Calculator, Marrero et al., 2016; 0 mm  $\text{ka}^{-1}$  erosion, LM scaling scheme). (D) Sample photograph for MUL01 (2018), with its corresponding mean Schmidt hammer R-value ( $\pm$  standard error of the mean).

### Landform/Region

Name of the associated moraine, or sampling region.

### Publication

Name of publication (Pallàs et al., 2006, 2010; Rodés, 2008; Delmas et al., 2008; Palacios et al., 2015; Crest et al., 2017).

### Isotope

$^{10}\text{Be}$  or  $^{36}\text{Cl}$ .

### Facility

Either Tandetron (Gif-sur-Yvette, France), ASTER (Aix-en-Provence, France) or PRIME (Purdue University, United States).

### SH\_Mean

Mean of 30 Schmidt hammer R-values. No outliers were removed following Niedzielski et al. (2009).

**SH\_SEM**

Standard error of the mean of 30 Schmidt hammer R-values.

**SH\_Sample\_Name**

If this surface was resampled with the Schmidt hammer, the corresponding sample name is listed here.

**CRONUS\_Age [Year\_Month\_Day]** The sample exposure age (ka), and the calculation date.

**CRONUS\_Internal [Year\_Month\_Day]** The internal exposure age uncertainty (ka), and the calculation date.

**CRONUS\_External [Year\_Month\_Day]** The external exposure age uncertainty (ka), and the calculation date.

## 2.2 Supplementary Table 3

### Sample name

Unique identifier for each boulder.

### Landform

Name of the associated moraine, following the prior work of Pallàs et al. (2006), Rodés (2008) and Palacios et al. (2015).

### Sub-Landform

Identifier to distinguish between the outer and inner Soum d'Ech moraines.

### Latitude\_DD

Sample latitude in decimal degrees ( $^{\circ}$ ).

### Longitude\_DD

Sample longitude in decimal degrees ( $^{\circ}$ ).

### Elevation\_m

Sample elevation in meters above sea level (m a.s.l), as measured using a handheld GPS.

### SH\_Mean

Mean of 30 Schmidt hammer R-values. No outliers were removed following Niedzielski et al. (2009).

### SH\_MAD

Mean absolute deviation of 30 Schmidt hammer R-values.

### SH\_SEM

Standard error of the mean of 30 Schmidt hammer R-values.

### TCN\_Sample\_Name

If this boulder has previously been dated using  $^{10}\text{Be}$  or  $^{36}\text{Cl}$ , the name is listed here.

### Calibrated\_Age\_ka

Calibrated exposure age of the boulder (ka), calculated through interpolation of the TCN-SH calibration curve (see Fig. 2.2). This curve is derived from orthogonal distance regression (ODR; Boggs and Rogers, 1990b) and is based on 54  $^{10}\text{Be}$  dated granite and granodiorite surfaces from the Pyrenees (Pallàs et al., 2006, 2010; Delmas et al., 2008; Crest et al., 2017) and their corresponding Schmidt hammer

R-values (Tomkins et al., 2018a). ODR allows for errors in both the independent and dependent variables. Here, we explicitly incorporate these errors ( $^{10}\text{Be}$  external age uncertainty; standard error of the mean (SEM) of the Schmidt hammer R-values) using a Monte Carlo style approach. This is described in pseudo code in Section 3, with full code available on GitHub: [https://github.com/matt-tomkins/moraine\\_paper\\_2020](https://github.com/matt-tomkins/moraine_paper_2020).

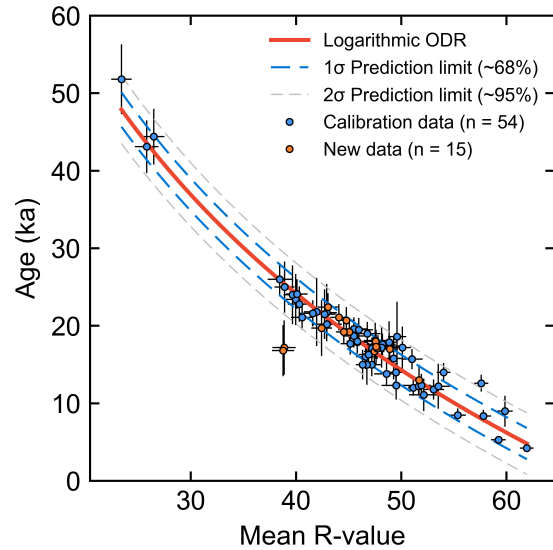


Figure 2.2: ODR TCN-SH calibration curve, based on 54  $^{10}\text{Be}$  dated granite and granodiorite surfaces from the Pyrenees (blue circles; Tomkins et al., 2018a). New data from the studied moraines ( $n = 15$ ) are shown as orange circles. Outliers ( $n = 2$ ) are not shown for clarity (see Page 2). For all samples, vertical error bars represent the external age uncertainty, while horizontal error bars represent the standard error of the mean (SEM) of 30 Schmidt hammer R-values.

This approach has now been implemented on SHED-Earth (<http://shed.earth>), an online calculator developed to enable wider and more consistent application of our approach (Tomkins et al., 2018b).

### **Calibrated\_Uncertainty\_ka**

The associated uncertainty (ka), derived from a  $1\sigma$  prediction limit. This prediction limit was calculated using the ODR covariance matrix (Boggs and Rogers, 1990a).

### **A\_axis\_cm**

Length of the longest boulder axis (cm).

### **B\_axis\_cm**

Length of the intermediate boulder axis (cm).

**C\_axis\_cm**

Length of the shortest boulder axis (cm).

**Ground\_Height\_cm**

Maximum height of boulder above the ground (cm).

**Volume\_m3**

Approximate volume of boulder ( $V$ , m<sup>3</sup>), calculated as the product of the axis lengths (m) as follows:

$$V = ABC$$

**Surface\_area\_m2**

Approximate surface area of boulder ( $S$ ; m<sup>2</sup>), calculated from the axis lengths (m) as follows:

$$S = 2(AB) + 2(AC) + 2(BC)$$

**Sphericity**

Boulder sphericity ( $\psi$ ), as defined by Wadell (1935), calculated using boulder volume ( $V$ ) and surface area ( $S$ ) as follows:

$$\Psi = \frac{\pi^{\frac{1}{3}}(6S)^{\frac{2}{3}}}{A}$$

**Mass\_Tonnes**

Approximate mass of the boulder in tonnes ( $T$ ), calculated using boulder volume ( $V$ ) and assuming a bulk density of 2.69 g cm<sup>3</sup>( $D$ ) as follows:

$$T = VD$$

### **Landform\_Age\_ka**

Age of the landform (ka), calculated using the Probabilistic Cosmogenic Age Analysis Tool (P-CAAT Version 1.0; Dortch et al., 2019). This method utilises non-linear curve fitting and a Monte Carlo style approach to isolate component Gaussian distributions to account for positive (prior exposure) and negative skew (incomplete exposure) of age datasets. This tool is based on earlier work by Dortch et al. (2013) and Murari et al. (2014).

### **Landform\_Uncertainty\_ka**

Uncertainty (ka) of the landform age. This estimate is derived from the  $1\sigma$  bounds of the isolated component Gaussian distribution.

### **Relative\_Difference\_ka**

Relative difference between the calibrated exposure age of the boulder and the age of the landform (ka).

### **Absolute\_Difference\_ka**

Absolute difference between the calibrated exposure age of the boulder and the age of the landform (ka).

### **Class\_95**

Boulder class (“Young”, “Good”, “Old”) as defined by the  $2\sigma$  uncertainty bounds ( $U$ ; ~95%) of the landform age ( $L$ , ka; see Fig. 2.3). These are distinguished as follows:

$$Young < L - U$$

$$Good \geq L - U \mid \leq L + U$$

$$Old > L + U$$

### **General\_Class\_95**

Boulder class (“Good”, “Bad”) as defined by the  $2\sigma$  uncertainty bounds ( $U$ ; ~95%) of the landform age ( $L$ , ka; see Fig. 2.3). These are distinguished as follows:

$$Good \geq L - U \mid \leq L + U$$

$$Bad < L - U \mid > L + U$$

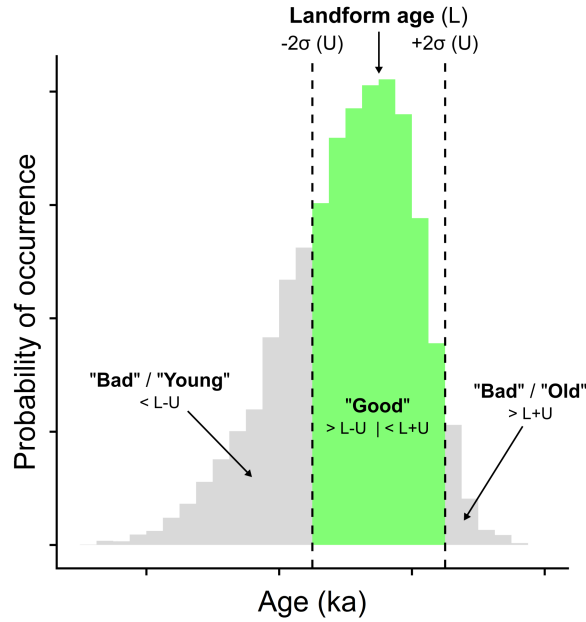


Figure 2.3: Boulder class, as defined by the  $2\sigma$  uncertainty bounds ( $U$ ) of the landform age ( $L$ ). “Good” boulders are those which fall within  $\pm 2\sigma$  (green shading), while “bad” boulders (“Young” / “Old”) are  $> 2\sigma$  from the landform age (grey shading).

### **Moraine\_Group**

Boulder group, either moraine crest (C), the inner ice-proximal slope (IS) or the outer ice-distal slope (OS).

### **AB | AC\_Ratio**

Ratio of longest ( $A$ ) to intermediate ( $B$ ) or shortest axes ( $C$ ).

### **Moss**

Approximate boulder coverage by moss or surface vegetation (0%, 20%, 40%, 60%, 80%, 100%). Note, Schmidt hammer sampling was conducted in areas free of moss or surface vegetation.

### **Lichen**

Binary category for lichen coverage (0 = Lichen absent, 1 = Lichen present). Note, Schmidt hammer sampling was conducted in lichen free areas following Matthews and Owen (2008).

### **Embedded**

Approximate percentage of boulder embedded in ground (0%, 20%, 40%, 60%, 80%, 100%).

### **Angularity**

Boulder morphology: Angular (A), Sub-angular (SA), Sub-rounded (SR) or Rounded (R).

### **Fractured**

Qualitative assessment of the degree of fracturing, defined as follows:

- 0 = no fractures.
- 0.25 = minor fractures.
- 0.5 = some fractures.
- 0.75 = major fractures.
- 1 = predominantly fractured.

Note, Schmidt hammer sampling was conducted away from fractures or surface discontinuities following Williams and Robinson (1983).

### **Matrix**

Characteristics of the underlying material, defined as follows:

- 0 = soil or sediment (i.e. matrix supported)
- 0.5 = combination of matrix and clast support e.g. sediment and boulders *or* cobbles with tightly packed sediment.
- 1 = boulders or cobbles (i.e. clast supported)

### **Slope\_Angle\_deg**

Angle ( $^{\circ}$ ) of the underlying slope.

### **Distance | Height\_percent**

These variables provide spatially-normalised information on the relative position of each boulder (*see* Fig. 2.4). For each sampled boulder, measurement points ( $n = 2$ ) were defined as the closest points along polylines digitised on (i) the moraine crest and (ii) the base of the moraine slope (*see* below). In turn, distance percent ( $D$ ) was calculated as follows:

$$D = \frac{C_d}{C_d + B_d}$$

where  $C_d$  is defined as the distance from the boulder to the moraine crest and  $B_d$  is defined as the distance from the boulder to the base of the moraine. Values can range from 0 for boulders located on the moraine crest to 1 for boulders on the margins of the moraine. In a similar fashion, height percent ( $H$ ) was calculated as follows:

$$H = \frac{S_h - B_h}{C_h - B_h}$$

where  $S_h$  is defined as the elevation of the sampled boulder,  $C_h$  is defined as the elevation of the moraine crest and  $B_h$  is defined as the elevation of the moraine base. Values can range from 0 for boulders at the base of the moraine to 1 for boulders located on the moraine crest. It should be noted that these values are not provided for a small number of boulders on the outer ice-distal slope of the Soum d'Ech outer moraine ( $n = 12$ ). This primarily reflects the subtle geomorphology of the Soum d'Ech site, where the precise boundary between the ice-distal moraine margin and the underlying topography is not clear.

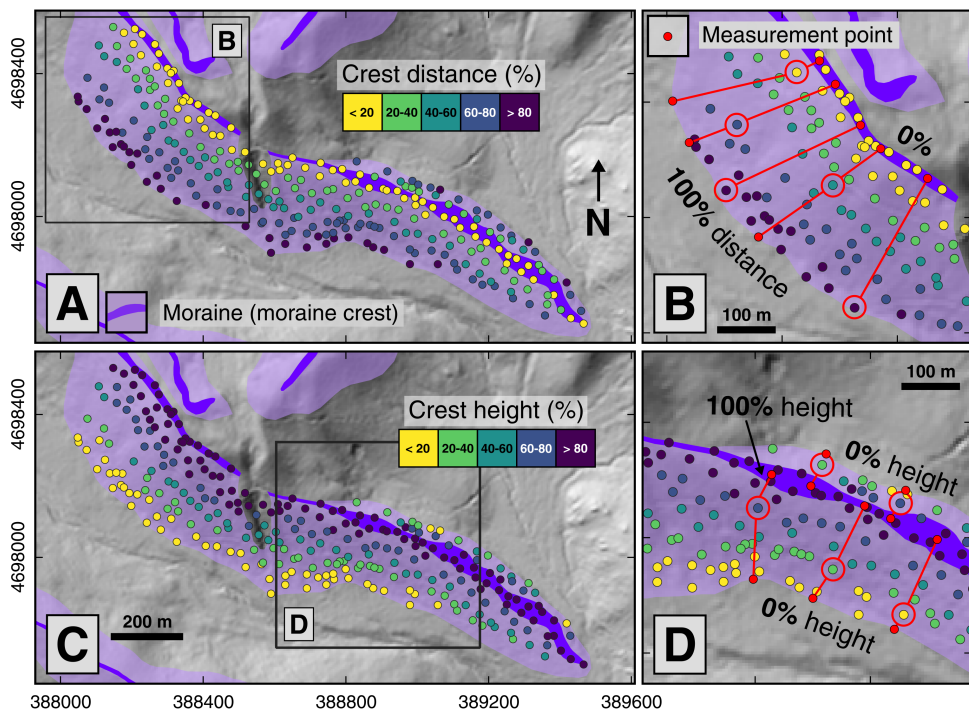


Figure 2.4: Relative boulder positions, as illustrated using data from the Arànsar left moraine. Sampled boulders ( $n = 275$ ) are plotted as circles and are coloured by distance percent (A) and height percent (C). Inset maps (B, D) illustrate the locations of measurement points for a subset of boulders (circled in red, linked by red lines).

**Crest | Base\_distance\_m**

Minimum distance between the sampled boulders and polylines (.shp) digitised along the moraine crest | moraine base (m).

**Crest | Base | Boulder\_height\_m**

Elevation of the moraine crest | moraine base | sampled boulder (m a.s.l). For consistency, measurements are derived from a ~5 m DEM from the Instituto Geográfico Nacional for the Aràns, Outer Pleta Naua and Tallada moraines. For the Soum d'Ech moraines, no data of comparable resolution are available so measurements are derived from ~30 m ASTER data (ASTER GDEM V3).

# 3 | Monte Carlo ODR

---

**Algorithm 1** Monte Carlo simulated Orthogonal Distance Regression (ODR)

---

**Require:**

$x \text{ data} \leftarrow SH \text{ mean}$   
 $x \text{ error} \leftarrow \pm SEM$   
 $y \text{ data} \leftarrow TCN \text{ age (ka)}$   
 $y \text{ error} \leftarrow \pm External \text{ uncertainty}$   
 $input \leftarrow values \text{ to predict for}$  ▷ e.g.  $SH(30, 40, 50, 60)$

```

1: procedure ( $x \text{ data}, x \text{ error}, y \text{ data}, y \text{ error}, input$ )
2:   for  $i \leftarrow 1 : 1000$  do ▷ 1000 iterations
3:      $x \leftarrow randomise(x \text{ data}, x \text{ error})$  ▷ ( $mean, \sigma$ )
4:      $y \leftarrow randomise(y \text{ data}, y \text{ error})$ 
5:     for  $i \leftarrow 1 : \infty$  do ▷ Loops until residuals  $< 2\sigma$ 
6:        $OLS \text{ model}(log10(x), y)$  ▷ Ordinary least squares
7:        $s \leftarrow OLS(studentised \text{ residuals})$ 
8:       if  $s > 2\sigma$  then
9:          $x, y \leftarrow x, y - s$  ▷ Trim outlier
10:      else
11:         $OLS \beta \leftarrow OLS(slope, intercept)$ 
12:      end if
13:    end for
14:     $ODR(log10(x), y, OLS \beta)$  ▷ Run ODR model
15:     $c[i] \leftarrow ODR(\beta, cov. matrix, residuals)$  ▷ Store ODR coefficients
16:  end for
17:   $A \leftarrow median(c)$  ▷ Aggregate ODR coefficients
18:  Predicted value  $\leftarrow predict(A\beta[slope] * log10(input) + A\beta[intercept])$ 
19:  Prediction interval  $\leftarrow interval(model \text{ function } (y = m * log10(x) + c), model \text{ derivatives},$ 
input, predicted values,
significance level (1 $\sigma$ , 2 $\sigma$ , 3 $\sigma$ ),
A[\beta, residuals, covariance matrix])
20: end procedure

```

---

Our analytical approach is based on logarithmic orthogonal distance regression (ODR; Boggs and Rogers, 1990b), implemented in Python SciPy (“scipy.odr”; <https://docs.scipy.org/doc/scipy/reference/odr.html>). This approach minimises orthogonal residuals to account for the possibility of measurement uncertainties in both the independent and dependent variables. In contrast, ordinary least squares regression assumes that the independent variable is measured without error.

An *unweighted* approach returns prediction estimates ( $1\sigma$ ) of  $\pm 1.6 - 1.8$  ka (calculated using the ODR covariance matrix; Boggs and Rogers, 1990a), with a distribution that corresponds to the empirical rule ( $\sim 70\%$  of calibration data within  $1\sigma$  interval,  $\sim 96\%$  within  $2\sigma$ , 100% within  $3\sigma$ ). However, the  $^{10}\text{Be}$  TCN ages ( $n = 54$ ) and their corresponding SH R-values have unique measurement uncertainties which should be incorporated explicitly (TCN  $\pm$  external age uncertainty; SH  $\pm$  Standard Error of

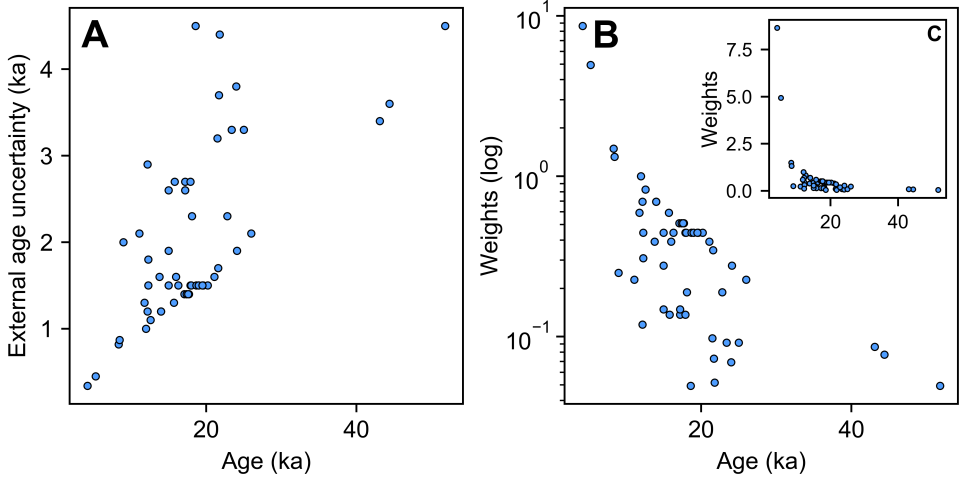


Figure 3.1: TCN age-uncertainty collinearity. (A) Correlation between 54 <sup>10</sup>Be TCN ages and their external uncertainties ( $u$ ). Use of external uncertainties is justified here because <sup>10</sup>Be concentrations were measured at different AMS laboratories (Jull et al., 2015). Collinearity is maintained when these data are converted into weights ( $\frac{1}{u^2}$ ), as shown with logged (B) and unlogged axes (C).

the Mean). This could be achieved using a *weighted* ODR, in which individual data points are weighted by their corresponding uncertainties. In turn, data points with high precision are weighted more heavily than those with low precision, and exert a larger influence on the final model coefficients.

However, this approach is not appropriate here because it requires unnecessary assumptions regarding weighting constants, which have a large effect on the weighting profile. For example, “scipy.odr” converts uncertainties ( $u$ ) into weights as follows:

$$\frac{1}{u^2}$$

Crucially, however, weighed regression also incorporates the ratio of variabilities ( $\lambda$ ):

$$\lambda = \frac{vX}{vY}$$

when  $vX$  is the error variance of the X data, and  $vY$  is the error variance of the Y data. In turn, using a weighted regression requires additional assumptions about the *relative* significance of errors. This is particularly challenging when the studied variables are measured in different units (i.e exposure age, SH R). Finally, weighting is complicated by TCN age-uncertainty collinearity (see Fig. 3.1; as age  $\nearrow$ , uncertainty  $\nearrow$ ; Ivy-Ochs et al., 2007; Dortch et al., 2019).

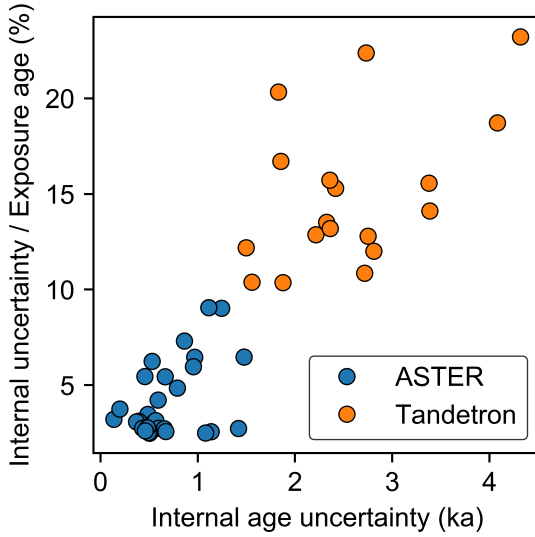


Figure 3.2:  $^{10}\text{Be}$  TCN measurement uncertainties. Internal age uncertainties plotted as a proportion of exposure age (%).  $^{10}\text{Be}$  concentrations were measured at the Tandetron AMS facility of Gif-sur-Yvette, France (Raisbeck et al., 1994) or at the ASTER AMS facility of Aix-en-Provence, France.

Instead, we use a Monte Carlo style approach with  $10^4$  iterations to explicitly incorporate measurement uncertainties, as described in pseudo code above and provided in full at [https://github.com/matt-tomkins/moraine\\_paper\\_2020](https://github.com/matt-tomkins/moraine_paper_2020). First, random samples are drawn from a normal (Gaussian) distribution based on the input data (Lines 3-4; TCN  $\pm$  external age uncertainty; SH  $\pm$  Standard Error of the Mean). In turn, these data are used to construct a logarithmic ordinary least squares regression (OLS; Line 6). The OLS  $\beta$  coefficients (slope, intercept) are used as initial parameters for the ODR model (Line 14).

However, a number of input values have considerable internal measurement uncertainties ( $\geq 10\%$  of exposure age; *see* Fig. 3.2) due to the lower analytical precision of earlier Tandetron Accelerator Mass Spectrometry (Raisbeck et al., 1994). As a result, these values can vary significantly when randomised. For example, sample CAC27 can range from  $\sim 6.4$  ka to  $\sim 18$  ka at  $2\sigma$  ( $12.2 \pm 2.9$  ka; Delmas et al., 2008; Crest et al., 2017). In turn, inclusion of these values can lead to quantitatively poor model fits. To account for this, we calculate internally studentised residuals for each OLS model (Line 7) and set a  $2\sigma$  threshold (95%) for excluding outliers (Line 9).

For each ODR model run ( $n = 10^4$ ), we record relevant model coefficients ( $\beta$ , covariance matrix and residuals). These values are aggregated by calculating the median (Line 17); a choice which is justified based on the distribution of coefficient values (*see* Fig. 3.3). Slope and intercept  $\beta$  values and maximum model residuals conform to a normal distribution, while covariance matrix values (*see* Boggs and Rogers, 1990a)

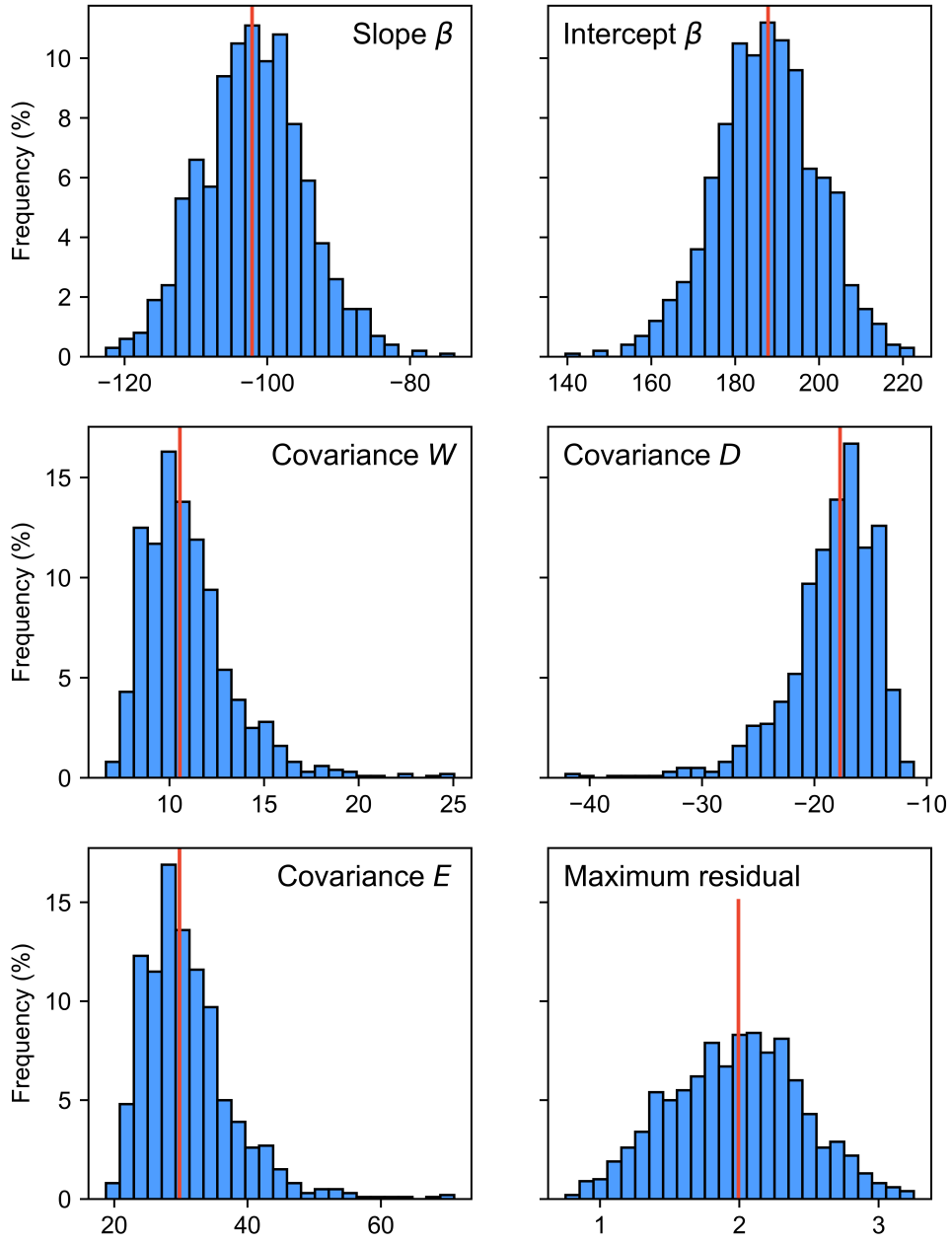


Figure 3.3: Simulated model coefficients ( $n = 10^4$ ) from Orthogonal Distance Regression ( $\beta$ , covariance matrix, residuals)

show some positive and negative skew. In turn, the median is an appropriate measure of central tendency as it is less sensitive to non-normal bias.

Using these aggregated coefficients, values can be predicted (Line 18) as follows:

$$\beta[\text{slope}] \cdot \log_{10}(x) + \beta[\text{intercept}]$$

where  $x$  is the input value. Finally, prediction intervals can be calculated (Line 19) by incorporating the model derivatives, a set significance level ( $1\sigma$ ,  $2\sigma$ ,  $3\sigma$ ) and the aggregated model coefficients ( $\beta$ , covariance matrix and residuals) following Boggs and Rogers (1990a).

## 4 | $^{10}\text{Be}$ analysis

10 boulders were selected on the Arànsa right moraine for  $^{10}\text{Be}$  analysis (see Fig. 4.1). Initial sampling was conducted in [Month Year], while SH sampling was conducted in August 2018 (Arànsa left) and November 2019 (Arànsa right). Sample treatment was performed in the Cosmogenic Isotope Laboratory at the Universitat de Barcelona. Samples were crushed and sieved to extract the 0.25–1 mm granulometric fraction. Minerals other than quartz were dissolved by HCl and H<sub>2</sub>SiF<sub>6</sub>, and remaining quartz grains were cleaned using sequential HF dissolutions to remove any potential atmospheric  $^{10}\text{Be}$  (Brown et al., 1991; Kohl and Nishiizumi, 1992; Cerling and Craig, 1994). Between 15 and 30 g per sample of clean quartz cores were then completely dissolved in HF and spiked with 300 mg of  $^9\text{Be}$  carrier (Brown et al., 1992). Beryllium was separated by successive solvent extractions and alkaline precipitations (Brown et al., 1992).

Measurements of  $^{10}\text{Be}$  concentrations were performed at the ASTER AMS facility of Aix-en-Provence, France. The measured  $^{10}\text{Be}/^9\text{Be}$  ratios were corrected for procedural blanks and calibrated against the National Institute of Standards and Technology standard reference material 4325 by using an assigned value of  $2.79 \pm 0.03 \times 10^{-11}$  and using a  $^{10}\text{Be}$  half-life of  $1.36 \pm 0.07 \times 10^6$  years (Nishiizumi et al., 2007). Analytical uncertainties (reported as  $1\sigma$ ) include uncertainties associated with AMS counting statistics, AMS external error and chemical blank measurement.  $^{10}\text{Be}$  concentrations in quartz were calculated following Balco (2006) and exposure ages calculated using the CRONUS Earth Web Calculator (Marrero et al., 2016). All ages are reported with no correction for erosion or snow cover to ensure that they are treated as minimum ages of exposure.

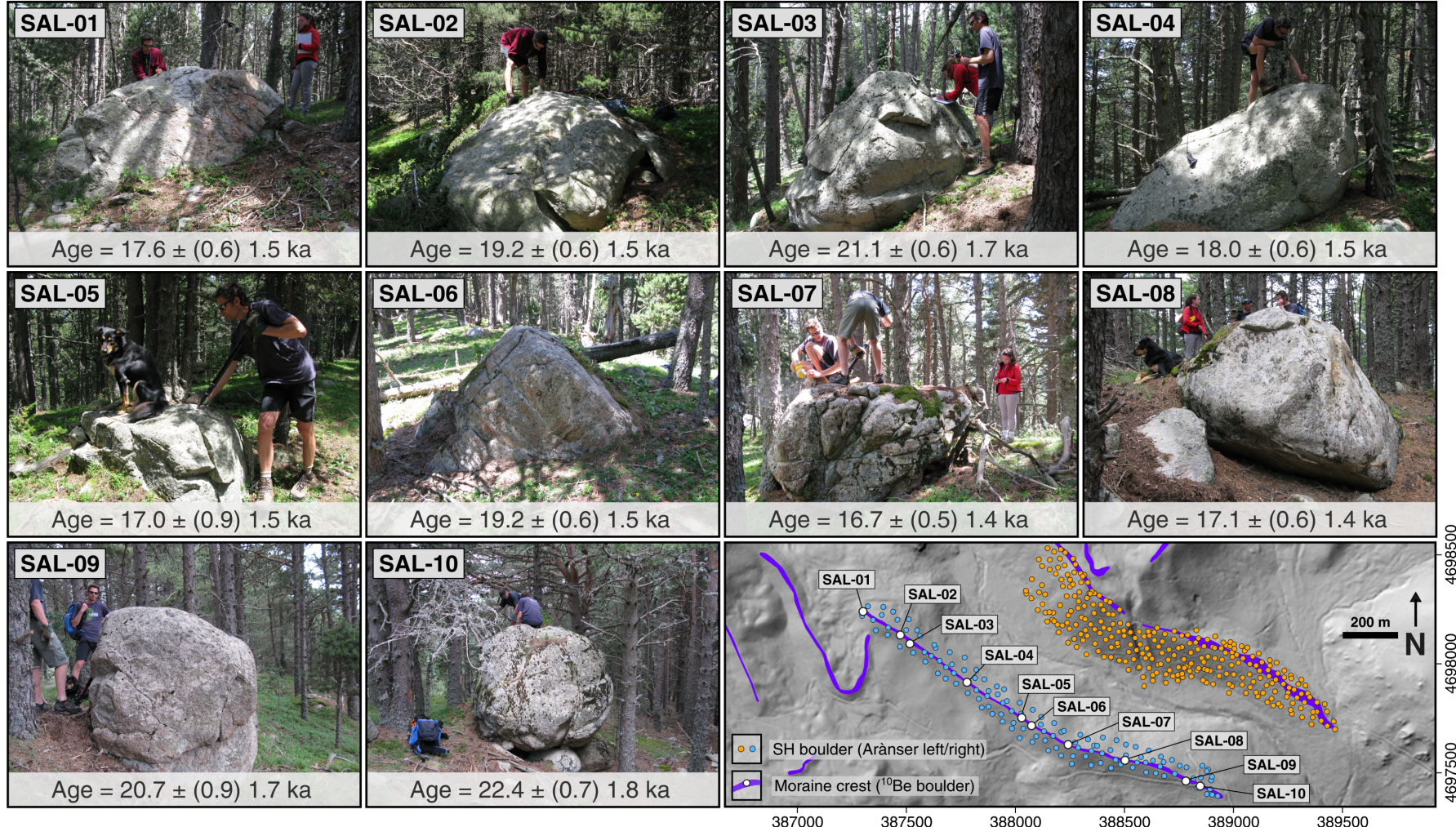


Figure 4.1: Sample photos of  $^{10}\text{Be}$  dated boulders on the Arànsler right moraine (SAL-01 to SAL-10) and their corresponding exposure ages (ka)  $\pm$  (internal) external uncertainties. Their locations are shown on the inset map (Topographic hillshade based on a  $\sim 5$  m DEM from the Instituto Geográfico Nacional), in addition to SH sampled boulders on the Arànsler left (orange points;  $n = 275$ ) and right moraines (blue circles;  $n = 130$ ).

# Bibliography

- Balco, G. Converting Al and Be isotope ratio measurements to nuclide concentrations in quartz. Technical report, Cosmogenic Nuclide Lab, University of Washington.
- Boggs, P. T. and Rogers, J. E. The Computation and Use of the Asymptotic Covariance Matrix for Measurement Error Models. Technical Report Internal Report 89-4102, National Institute of Standards and Technology, Gaithersburg, MD, Applied and Computational Mathematics Division.
- Boggs, P. T. and Rogers, J. E. Orthogonal distance regression. In "*Statistical analysis of measurement error models and applications: proceedings of the AMS-IMS-SIAM joint summer research conference held June 10-16, 1989,*", volume 12, page 186, 1990, doi:10.6028/nist.ir.89-4197.
- Brown, E. T., Edmond, J. M., Raisbeck, G. M., Yiou, F., Kurz, M. D., and Brook, E. J. Examination of surface exposure ages of Antarctic moraines using *in situ* produced  $^{10}\text{Be}$  and  $^{26}\text{Al}$ . *Geochimica et Cosmochimica Acta*, 55(8):2269–2283, 1991, doi:10.1016/0016-7037(91)90103-C.
- Brown, E. T., Brook, E. J., Raisbeck, G. M., Yiou, F., and Kurz, M. D. Effective attenuation lengths of cosmic rays producing  $^{10}\text{Be}$  and  $^{26}\text{Al}$  in quartz: Implications for exposure age dating. *Geophysical Research Letters*, 19(4):369–372, 1992, doi:10.1029/92GL00266. \_eprint: <https://agupubs.onlinelibrary.wiley.com/doi/pdf/10.1029/92GL00266>.
- Cerling, T. E. and Craig, H. Geomorphology and *in-situ* cosmogenic isotopes. *Annual Review of Earth and Planetary Sciences*, 22(1):273–317, 1994, doi:10.1146/annurev.ea.22.050194.001421. \_eprint: <https://doi.org/10.1146/annurev.ea.22.050194.001421>.
- Crest, Y., Delmas, M., Braucher, R., Gunnell, Y., and Calvet, M. Cirques have growth spurts during deglacial and interglacial periods: Evidence from  $^{10}\text{Be}$  and  $^{26}\text{Al}$  nuclide inventories in the central and eastern Pyrenees. *Geomorphology*, 278:60–77, 2017, doi:10.1016/j.geomorph.2016.10.035.
- Delmas, M., Gunnell, Y., Braucher, R., Calvet, M., and Bourlès, D. Exposure age chronology of the last glaciation in the eastern Pyrenees. *Quaternary Research*, 69(2):231–241, 2008, doi:10.1016/j.yqres.2007.11.004.
- Dortch, J., Saha, S., Tomkins, M. D., Murari, M. K., Schoenbohm, L. M., and Curl, D. Probability-based interpretation of terrestrial cosmogenic radionuclide ages: P-CAAT, a tool for the ages. AGU, 2019, doi:<https://agu.confex.com/agu/fm19/meetingapp.cgi/Paper/502207>.
- Dortch, J. M., Owen, L. A., and Caffee, M. W. Timing and climatic drivers for glaciation across semi-arid western Himalayan–Tibetan orogen. *Quaternary Science Reviews*, 78:188–208, 2013, doi:10.1016/j.quascirev.2013.07.025.
- Ivy-Ochs, S., Kerschner, H., and Schlüchter, C. Cosmogenic nuclides and the dating of Lateglacial and Early Holocene glacier variations: The Alpine perspective. *Quaternary International*, 164–165:53–63, 2007, doi:10.1016/j.quaint.2006.12.008.
- Jull, A. J. T., Scott, E. M., and Bierman, P. The CRONUS-Earth inter-comparison for cosmogenic isotope analysis. *Quaternary Geochronology*, 26:3–10, 2015, doi:10.1016/j.quageo.2013.09.003.
- Kohl, C. P. and Nishiizumi, K. Chemical isolation of quartz for measurement of *in-situ* -produced cosmogenic nuclides. *Geochimica et Cosmochimica Acta*, 56(9):3583–3587, 1992, doi:10.1016/0016-7037(92)90401-4.
- Marrero, S. M., Phillips, F. M., Borchers, B., Lifton, N., Aumer, R., and Balco, G. Cosmogenic nuclide systematics and the CRONUScalc program. *Quaternary Geochronology*, 31:160–187, 2016, doi:10.1016/j.quageo.2015.09.005.
- Matthews, J. A. and Owen, G. Endolithic lichens, rapid biological weathering and schmidt hammer r-values on recently exposed rock surfaces: storbreen glacier foreland, jotunheimen, norway. *Geografiska Annaler: Series A, Physical Geography*, 90(4):287–297, 2008, doi:10.1111/j.1468-0459.2008.00346.x.

- Murari, M. K., Owen, L. A., Dortch, J. M., Caffee, M. W., Dietsch, C., Fuchs, M., Haneberg, W. C., Sharma, M. C., and Townsend-Small, A. Timing and climatic drivers for glaciation across monsoon-influenced regions of the Himalayan–Tibetan orogen. *Quaternary Science Reviews*, 88:159–182, 2014, doi:10.1016/j.quascirev.2014.01.013.
- Niedzielski, T., Migoń, P., and Placek, A. A minimum sample size required from Schmidt hammer measurements. *Earth Surface Processes and Landforms*, 34(13):1713–1725, 2009, doi:10.1002/esp.1851.
- Nishiizumi, K., Imamura, M., Caffee, M. W., Southon, J. R., Finkel, R. C., and McAninch, J. Absolute calibration of  $^{10}\text{Be}$  AMS standards. *Nuclear Instruments and Methods in Physics Research Section B: Beam Interactions with Materials and Atoms*, 258(2):403–413, 2007, doi:10.1016/j.nimb.2007.01.297.
- Palacios, D., Gómez-Ortiz, A., Andrés, N., Vázquez-Selem, L., Salvador-Franch, F., and Oliva, M. Maximum extent of Late Pleistocene glaciers and last deglaciation of La Cerdanya mountains, Southeastern Pyrenees. *Geomorphology*, 231:116–129, 2015, doi:10.1016/j.geomorph.2014.10.037.
- Pallàs, R., Rodés, Á., Braucher, R., Carcaillet, J., Ortuño, M., Bordonau, J., Bourlès, D., Vilaplana, J. M., Masana, E., and Santanach, P. Late Pleistocene and Holocene glaciation in the Pyrenees: a critical review and new evidence from  $^{10}\text{Be}$  exposure ages, south-central Pyrenees. *Quaternary Science Reviews*, 25(21):2937–2963, 2006, doi:10.1016/j.quascirev.2006.04.004.
- Pallàs, R., Rodés, Á., Braucher, R., Bourlès, D., Delmas, M., Calvet, M., and Gunnell, Y. Small, isolated glacial catchments as priority targets for cosmogenic surface exposure dating of Pleistocene climate fluctuations, southeastern Pyrenees. *Geology*, 38(10):891–894, 2010, doi:10.1130/G31164.1.
- Raisbeck, G. M., Yiou, F., Bourlès, D., Brown, E., Deboffle, D., Jouhanneau, P., Lestringuez, J., and Zhou, Z. Q. The AMS facility at Gif-sur-Yvette: progress, perturbations and projects. *Nuclear Instruments and Methods in Physics Research Section B: Beam Interactions with Materials and Atoms*, 92(1):43–46, 1994, doi:10.1016/0168-583X(94)95972-2.
- Rodés, Á. *La última deglacación en los pirineos: de superficies de exposición mediante  $^{10}\text{be}$ , y modelado numérico de paleoglaciares*. <http://purl.org/dc/dcmitype/Text>, Universitat de Barcelona. Pages: 1.
- Tomkins, M. D., Dortch, J. M., Hughes, P. D., Huck, J. J., Stimson, A. G., Delmas, M., Calvet, M., and Pallàs, R. Rapid age assessment of glacial landforms in the Pyrenees using Schmidt hammer exposure dating (SHED). *Quaternary Research*, 90(1):26–37, 2018, doi:10.1017/qua.2018.12.
- Tomkins, M. D., Huck, J. J., Dortch, J. M., Hughes, P. D., Kirkbride, M. P., and Barr, I. D. Schmidt Hammer exposure dating (SHED): Calibration procedures, new exposure age data and an online calculator. *Quaternary Geochronology*, 44:55–62, 2018, doi:10.1016/j.quageo.2017.12.003.
- Wadell, H. Volume, Shape, and Roundness of Quartz Particles. *The Journal of Geology*, 43(3):250–280, 1935, doi:10.1086/624298. Publisher: The University of Chicago Press.
- Williams, R. B. G. and Robinson, D. A. The effect of surface texture on the determination of the surface hardness of rock using the schmidt hammer. *Earth Surface Processes and Landforms*, 8(3):289–292, 1983, doi:10.1002/esp.3290080311.